Journal of Solid State Chemistry **157,** 309–323 (2001)
doi:10.1006/jssc.2000.9068, available online at http://www.idealibrary.com on IDEAL®

TEM Study of the Electron-Doped Layered $La_{2-2x}Ca_{1+2x}Mn_2O_7$: Orthorhombic Phase in the $0.8 < x < 1.0$ Composition Range

Leonid A. Bendersky

Metallurgy Division, NIST, 100 Bureau Drive, Stop 8554, Gaithersburg, Maryland 20899-8554

and

Rongji Chen, Ian D. Fawcett, and Martha Greenblatt

Department of Chemistry, Rutgers, The State University of New Jersey, Piscataway, New Jersey 08854

Received July 18, 2000; in revised form November 21, 2000; accepted December 8, 2000; published online February 19, 2001

A series of Ruddlesden–Popper compounds with $n = 2$ and stoichiometry $La_{2-2x}Ca_{1+2x}Mn_2O_7$ were synthesized by a citrate gel technique and studied by TEM for the composition range $0.8 < x < 1.0$. *In situ* experiments and analysis of substructure/twins identified structural changes of the *I*4/*mmm* phase at low temperatures (200–350°C). Reciprocal space analysis identified superlattice reflections (not previously detected by X ray) and possible space groups. The low-temperature phase belongs to the noncentrosymmetric $Cmc2_1$ or *Ama*2 space group, and the transient *Cmcm* space group is also possible. These structural transitions do not coincide with the magnetic transitions, which occur below room temperature. A structural model based on tilting of almost-rigid octahedra is suggested for *Cmcm* and $Cmc2_1$. The proposed model for the low-temperature $Cmc2_1$ phase has a $\Phi\Phi\Psi_z/\Phi\Phi\Psi_z$ combination of tilts, while the transient *Cmcm* has a $\Phi\Phi0/\Phi\Phi0$ combination of tilts. © 2001 Academic Press

Key Words: **$La_{2-2x}Ca_{1+2x}Mn_2O_7$; manganates; TEM; crystallography; phase transition.**

1. INTRODUCTION

Perovskite-based manganates have been the subject of intense research because of their complex magnetic and electric transport properties, especially colossal magnetoresistance (CMR) (1). In these materials the *A*-site cations (ideally 12-coordinated) of perovskite ABO_3 are usually a mixture of cations with 3 + (rare earth) and 2 + (alkaline earth) valences (e.g., La^{3+} and Sr^{2+}), which produces mixed-valence manganese (Mn^{3+} and Mn^{4+}) in the octahedrally coordinated *B*-site. The search for materials with larger CMR effects has led to the study of layered manganates, and in particular Ruddlesden–Popper (RP) structures with $(AO)(ABO_3)_n$ ($n = 1$, 2, and 3) stoichiometries (2). Indeed, the RP phases with $n = 2$, $Ln_{2-2x}Sr_{1+2x}Mn_2O_7$ ($0 < x < 0.4$), have shown strong CMR (3). The structures of the RP phases are comprised of perovskite-like blocks *n* octahedra thick separated by rock salt *A*O layers, Fig. 1. Similar to the three-dimensional (3D; $n = \infty$) perovskite manganates, the layered two-dimensional (2D) manganates also have complex magnetic and transport behavior as a function of composition and temperature. An additional component of the RP structures that affects their properties is their low-dimensionality (4). Therefore, the study of the properties and structures of layered manganates is of both fundamental and practical interest.

In our recent work, a series of $La_{2-2x}Ca_{1+2x}Mn_2O_7$ ($0.6 \le x \le 1.0$) ($n = 2$) RP phases was synthesized with a citrate gel technique (5). The $0.6 \le x \le 1.0$ range is in the electron-doped region, with a majority of Mn^{4+} ions in these mixed-valence manganates. According to measurements of magnetic susceptibility and conductivity, two distinctly different behaviors were found for compositions below and above $x = 0.8$. In the region $0.6 \le x \le 0.8$, the magnetic susceptibility has a pronounced inflection at ~280 K, presumably due to charge ordering, and antiferromagnetic order develops at lower temperatures (~150–200 K) with quasi-2D fluctuation effects above the ordering temperature (T_N). The magnetic properties are different for $0.825 \le x < 1.0$. At higher temperatures 2D magnetic coupling is observed and at ~115 K the system spontaneously orders antiferromagnetically, but with a ferromagnetic moment (canted antiferromagnetism). Since charge ordering leading to insulating behavior was suspected, a more detailed transmission electron microscopy (TEM) study was undertaken. This study found that the different magnetic behavior previously observed in the two regions, $0.6 \le x \le 0.8$ and $0.825 \le x < 1.0$, correlates with different structural characteristics, incommensurate 2D

0022-4596/01 $35.00
Copyright © 2001 by Academic Press
All rights of reproduction in any form reserved.

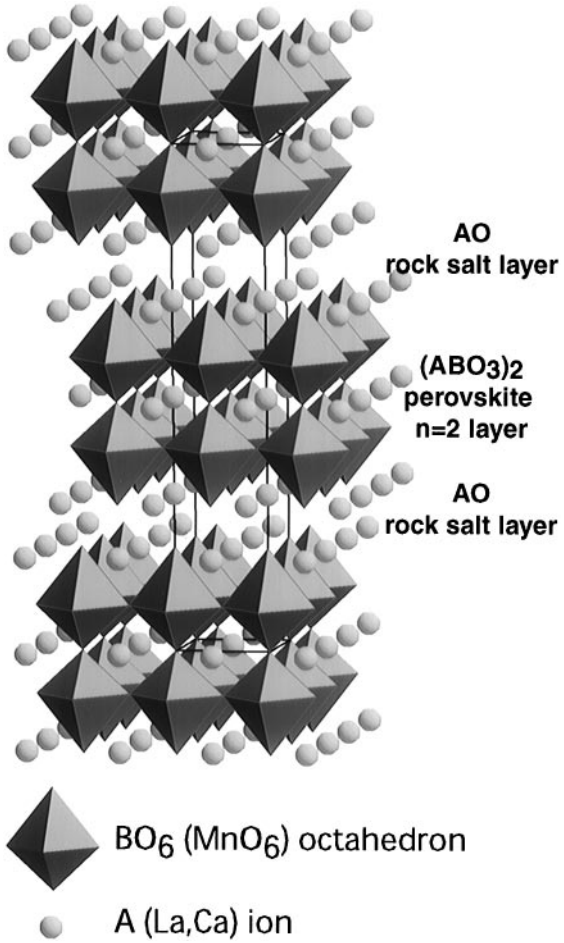

FIG. 1. Schematic representation of the Ruddlesden–Popper ($n = 2$) tetragonal $I4/mmm$ structure. The atomic coordinates are taken from Ref. (4).

modulation, and commensurate superlattice reflections, respectively. In this paper we report the study of $0.8 < x < 1.0$ compounds by electron diffraction and high-resolution imaging. The study of $0.6 < x \leq 0.8$ compounds will be published elsewhere (6).

2. EXPERIMENTAL PROCEDURES

Samples of $La_{2-2x}Ca_{1+2x}Mn_2O_7$ were prepared from La_2O_3 (Alfa Aesar, 99% dried in air at 800°C prior to use), $CaCO_3$ (Aldrich, 99+%), and $Mn(NO_3)_2$ (Aldrich, 49.7 wt% solution of dilute nitric acid) by a citrate gel technique. Details of the synthesis are described in the work of Fawcett *et al.* (5). The powder was sintered into pellets at 1250°C for 24 h and quenched to room temperature (RT) in air. Three specimens with compositions $x = 0.825$, 0.85, and 0.9 were studied in this work. The TEM specimens were prepared from the sintered pellets by conventional methods involving grinding, dimpling, and ion thinning. The specimens were examined using JEM3010 and Philips 430[1] TEM microscopes operated at 300 kV and 200 kV, respectively. *In situ* heating and cooling experiments were performed using double tilt specimen holders in the Phillips 430 microscope. In all specimens studied a small fraction of an amorphous phase, rich in carbon but including La, Ca, Mn, and O, was observed between the grains of the crystalline phase. The presence of the amorphous phase and difficulties in characterizing it introduce some uncertainties in the precise composition of the studied crystalline phase.

3. EXPERIMENTAL RESULTS

3.1. Establishing Reciprocal Lattice and Space Group

Figure 2a shows a bright-field image of a typical grain ($x = 0.825$ specimen) from which a selected area electron diffraction (SAD) pattern (Fig. 2b) was taken using a large selected area aperture. The SAD pattern is indexed as $[001]_t$ according to the tetragonal (t) lattice of an ideal $I4/mmm$ RP $n = 2$ structure ($a \approx 0.375$ nm and $c \approx 1.93$ nm (2, 4)). The $[001]_t$ pattern (as well as other SAD patterns shown later) is typical and common to all the specimens in the $0.8 < x < 1.0$ composition range. The difference from the ideal $I4/mmm$ structure lies in the presence of superlattice reflections $\frac{1}{2}\frac{1}{2}0$ and $\frac{1}{2}\frac{1}{2}0$ (reciprocal lattice vectors $k_1 = \frac{1}{2}[hh0]_t^*$ and $k_2 = \frac{1}{2}[h\bar{h}0]_t^*$ (throughout the paper we will use coordinates and indexes of the tetragonal $I4/mmm$, unless otherwise specified). Note that $k_1 + k_2 = \langle 100 \rangle^*$ reflections are very weak, which suggests that k_1 and k_2 are decoupled, i.e., come from two structural variants of symmetry lower than $I4/mmm$. This is confirmed by convergent beam microdiffractions (Figs. 2c, 2d) taken at different locations of the grain, which show either the k_1 or k_2 set of reflections (although it was difficult to completely eliminate the presence of a second set).

Convergent beam microdiffraction from a single variant taken at the $[110]_t$ zone axis for an $x = 0.825$ sample is shown in Fig. 3. The value of the first-order Laue zone (FOLZ) radius gives $H = 1/0.53\ \text{nm}^{-1}$ (H is a distance between the zero and first Laue zone). The rectangles on the image represent a cell of fundamental (tetragonal $I4/mmm$) spots centered with a superlattice reflection (solid line, ZOLZ; dashed, FOLZ). Translation of the cell from FOLZ to ZOLZ is also shown. The geometry of the reciprocal lattice deduced from Fig. 3 suggests an orthorhombic cell with approximate parameters $a_o = \sqrt{2}a_t = 0.52$ nm; $b_o = \sqrt{2}a_t = 0.52$ nm; $c_o = c_t = 1.93$ nm. The cell is confirmed by a set of SAD patterns taken in orientations including the c-axis by tilting a grain around the $[001]_t^*$ direction. The SAD patterns are presented in Fig. 4 and

[1] The use of brand or trade names does not imply endorsement of the product by NIST.

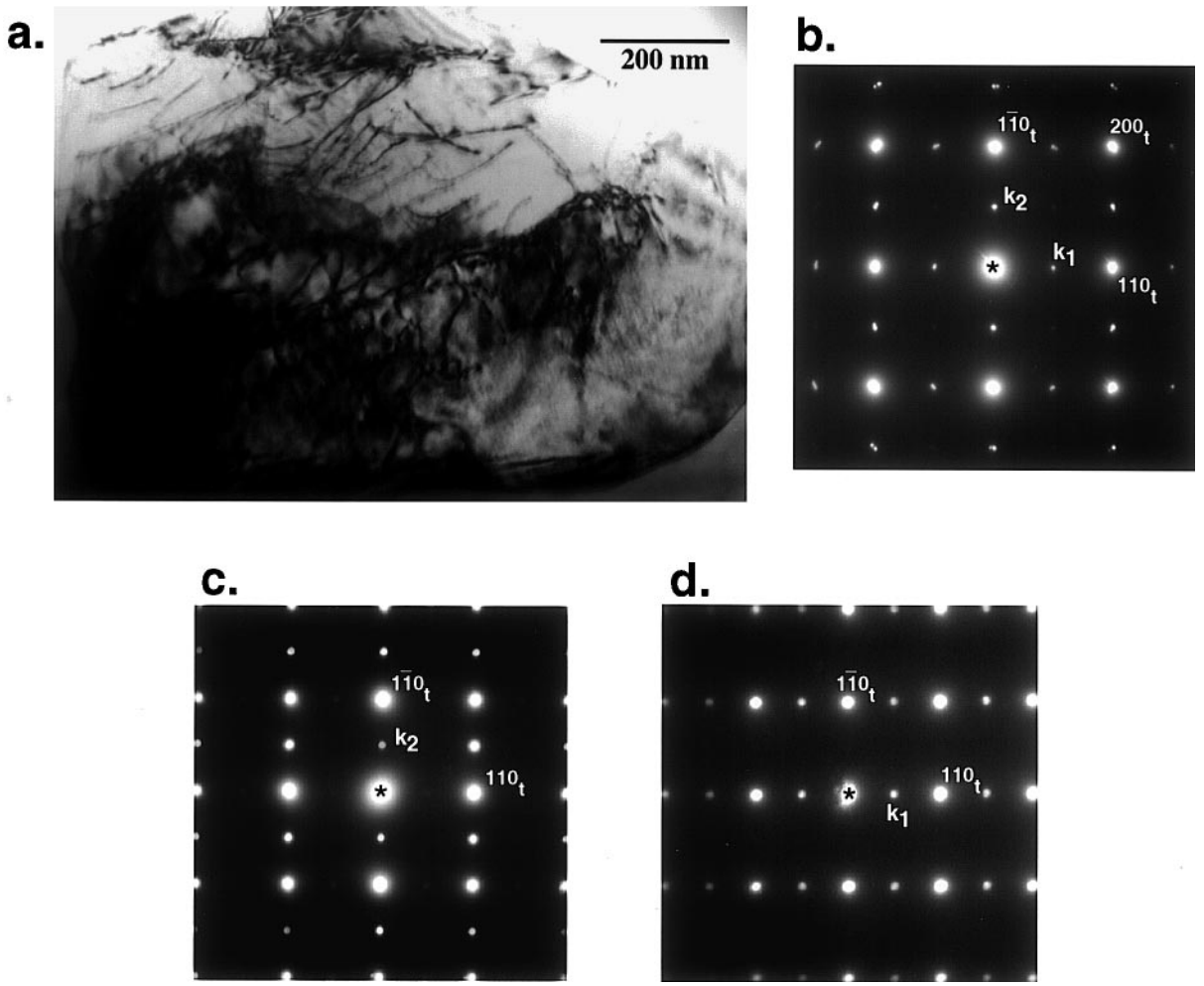

FIG. 2. (a) Bright-field image of a single grain ($x = 0.825$ specimen) from which a $[001]_t$ SAD pattern (b) was obtained using a large selected area aperture. (c, d) Microdiffraction patterns taken at different locations in the grain show that k_1 and k_2 reflections are not coupled. Note the prominent presence of dislocation-like defects in the grain.

indexed as (a) $[110]_t$, (b) $[010]_t$, and (c) $[1\bar{1}0]_t$ zone axes. Figure 4e shows the schematic drawing of the $[001]_t$ pattern and traces of vertical planes corresponding to the SAD patterns *a*–*c*. This set of SAD patterns corresponds to a variant with $k_2 = \frac{1}{2}[h\bar{h}0]_t^*$. The absence of $\frac{1}{2}(1\bar{1}0)_t$ reflections in the $[110]_t$ pattern, Fig. 4a, is due to extinction conditions, which are violated by double diffraction in the $[001]_t$ pattern, Fig. 2b. The effect of double diffraction is demonstrated in Fig. 4d, where the SAD pattern shown is obtained by tilting the $[110]_t$ direction (Fig. 4a) around $(1\bar{1}0)_t^*$ about 20°. Streaking along the $[00l]_t$ direction suggests the presence of (001) faults or intergrowths. The streaking (coming from FOLZ) also contributes to the visibility of the forbidden $\frac{1}{2}(110)_t$ type of reflections on the $[001]_t$ pattern.

Based on the electron diffraction results, the orthorhombic reciprocal lattice of a single variant is drawn schematically in Fig. 5, where the reciprocal lattice of the tetragonal *I*4/*mmm* is shown with dark circles. After taking into account the problem of double diffraction, the following set of reflection conditions for the orthorhombic structure was established: $00l$, $l = 2n$; $0k0$, $k = 2n$; $h00$, $h = 2n$; $hk0$, $h = 2n$; $h0l$, $h + l = 2n$; $0kl$, $k,l = 2n$; hkl, $h + l = 2n$. Consulting Table 3.2 of the reflection conditions for possible space groups in the *International Tables for Crystallography* (7), the space groups listed in Table 1 are suggested.

3.2. *High-Resolution Imaging*

Figure 6 shows high-resolution TEM images (HRTEM) of a structure with a $[001]_t$ orientation. Figure 6a shows an image of a single domain. Although it is difficult visually to see the doubling of (110) planes on the image, the corresponding fast Fourier transform (FFT) of the image clearly shows the presence of $k = \frac{1}{2}[110]_t^*$ scattering. In some instances the coexistence of ordered and disordered domains was also observed, as is demonstrated in Fig. 6b. In

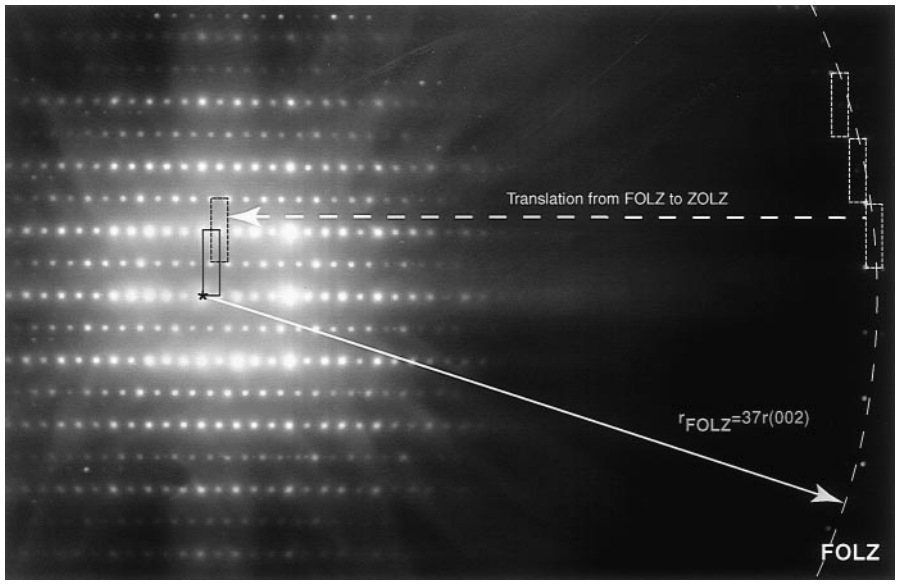

FIG. 3. Convergent beam microdiffraction pattern taken from a grain of $x = 0.825$ specimen oriented at the $[110]_t$ zone axis. Position of a first-order Laue zone (FOLZ) radius suggests $H = 1/0.53\ \text{nm}^{-1}$ (H is a distance between zero and the first Laue zone). The rectangles on the image represent a cell of fundamental (tetragonal) spots centered with a superlattice reflection (solid line, ZOLZ; dashed line, FOLZ).

this figure the boundary between the disordered (upper part B) and ordered (lower A) region is shown with a dashed line. The effect of ordering on the image contrast is very subtle, affecting only the variation in the intensity of the white dots. No visual changes in the location of white dots on a square net of perovskite lattice can be seen. According to image simulations for the $I4/mmm$ structure, in a wide range of defocus-thickness conditions (including near-Scherzer

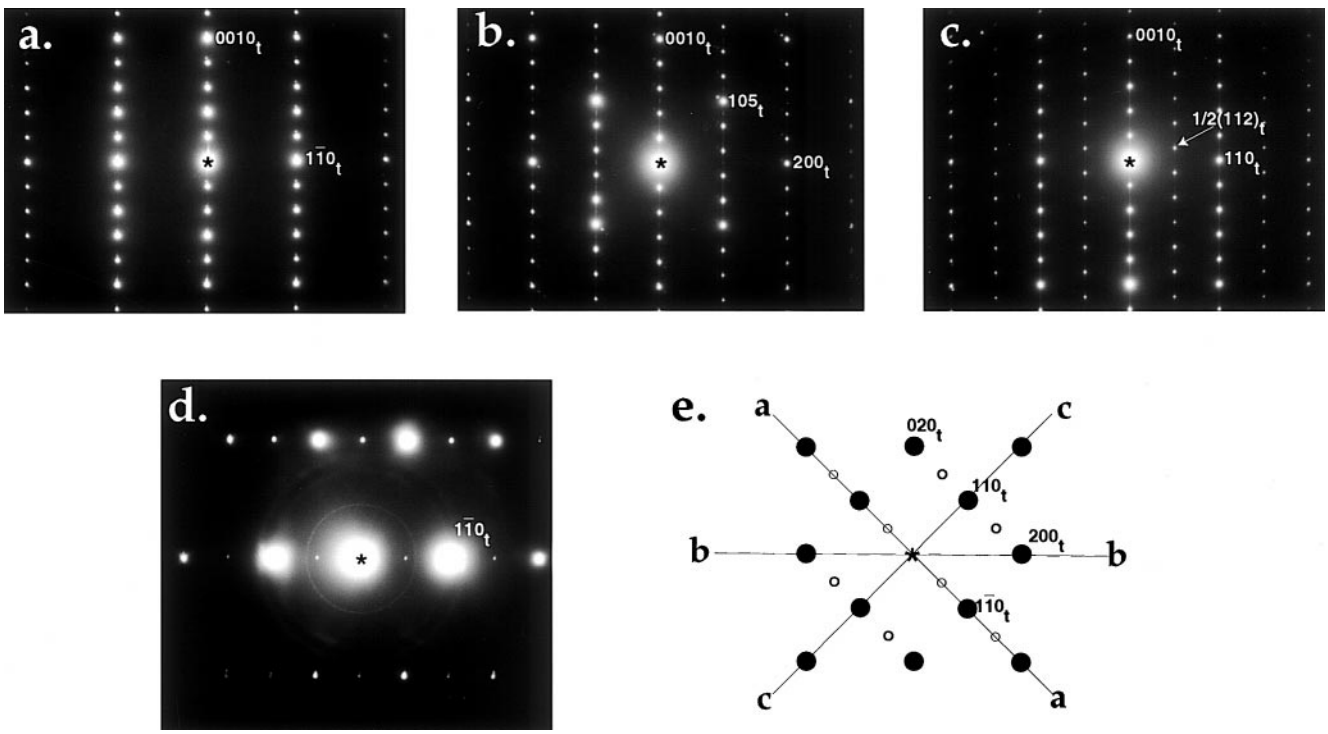

FIG. 4. SAD patterns taken from a $La_{2-2x}Ca_{1+2x}Mn_2O_7$ ($x = 0.85$) specimen and indexed as (a) $[110]_t$, (b) $[010]_t$, and (c) $[1\bar{1}0]_t$. (d) This SAD pattern was obtained by tilting the crystal in (a) orientation around $[1\bar{1}0]_t^*$ about 20°. (e) A schematic drawing of the $[001]_t$ pattern where the traces of vertical planes corresponding to the SAD patterns (a)–(c) are shown.

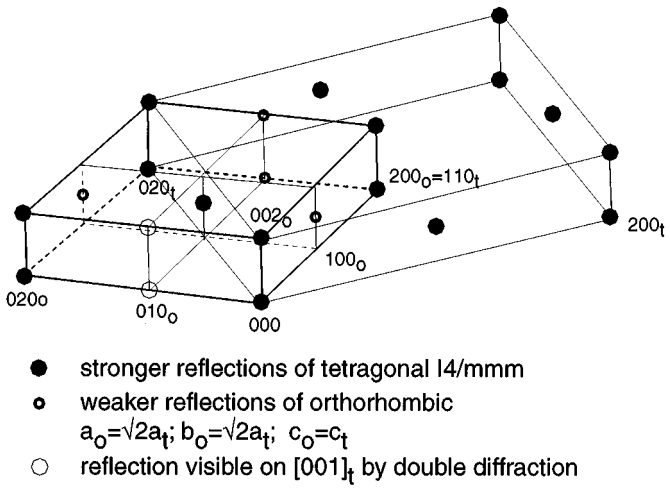

FIG. 5. Schematic drawing showing an orthorhombic reciprocal lattice of the $0.8 < x < 1.0$ phase according to the electron diffraction experiments. The lattice is derived from the tetragonal *I*4/*mmm* and has approximate parameters $a_o = \sqrt{2}a_t = 0.52$ nm; $b_o = \sqrt{2}a_t = 0.52$ nm; $c_o = c_t = 1.93$ nm. Dark-shaded circles represent fundamental reflections of the tetragonal *I*4/*mmm*; small empty circles, superlattice of the orthorhombic lattice; large empty circles, kinematically forbidden reflections but observed as a result of double diffraction.

defocus of the images in Fig. 6) the white dots correspond to columns of Mn/(La, Ca) ions.

The HRTEM image in the $[1\bar{1}0]_t$ orientation in Fig. 7 shows a perfect stacking of two-octahedra-thick ($n = 2$) layers. Doubling of the periodicity due to the $k = \frac{1}{2}\langle 110\rangle_t^*$ ordering can be seen only with the help of the FFT (shown in inset). Although Fig. 7 shows a perfect stacking of layers, a more typical picture shows the presence of intergrowth layers. Such a defected structure is shown in a low-magnification image, Fig. 8. Structural details of the intergrowth are similar to those of the $0.6 \leq x \leq 0.8$ specimens and will be presented elsewhere (6).

3.3. Substructure and Defects

Closer examination of the microstructure yields a subset of twinlike plates with planar interfaces normal to the *c*-direction, as shown in Fig. 9. Images in the figure are taken in the orientation close to the $[320]_t$ zone axis. The type of superlattice reflections in the SAD pattern, Fig. 9b, suggests a single-variant region (for a second variant, the row of superlattice reflections would be shifted by $[001]_t^*$). The presence of the substructure cannot be seen from either bright-field images (Fig. 9a, no apparent contrast) or a SAD pattern (Fig. 9b, no extra reflections or clear splitting of spots). The intensity streaking in the $[001]_t^*$ direction appears only along the row of superlattice reflections. However, the twin-like substructure became visible on dark-field images (Figs. 9c, 9d) obtained with an objective aperture positioned on the $(\frac{1}{2}\ \frac{3}{2}\ 0)_t$ row of superlattice reflections. By either a slight shift of the aperture or by specimen tilting only 1–2° it was possible to reverse the contrast of the twins. Such diffraction behavior suggests that the twins are "inversion twins," with a noncentrosymmetric structure. For such a structure, the variants related by inversion symmetry operation will have the same reciprocal lattice, but a different excitation error. Another possibility is the presence of very small distortions of the orthorhombic lattice (e.g., to a monoclinic lattice).

Although the presence of variants with different $k = \frac{1}{2}\langle 110\rangle_t^*$ was detected for the $[001]_t$ orientation using microdiffraction (Fig. 2), the morphology of the domains was not clear at this orientation. Better understanding of the morphology was obtained from dark-field imaging using superlattice reflections. Figure 10a shows such an image, where the twinlike structure was obtained in a region from which the SAD pattern, Fig. 10b, was taken. The position of the objective aperture is indicated on the pattern. Enlargement of a part of the SAD pattern shows the presence of variants, $k_1 = \frac{1}{2}\ [hh0]_t^*$ and $k_2 = \frac{1}{2}[h\bar{h}0]_t^*$, with overlapping nonequivalent fundamental reflections, e.g. $(420)_o$ and $(240)_o$ (o, orthorhombic lattice) in Fig. 10b.

3.4. In Situ Cooling and Heating Experiments

The changes in magnetic behavior at lower temperatures for compounds with $0.8 < x < 1.0$ suggested the possibility of low-temperature structural transition. The observation of a twinlike substructure suggests a structural transition

TABLE 1
Reflection Conditions (e.g., $h+l = 2n$) as Derived from Electron Diffraction and the Corresponding Space Groups

Reflection conditions							
hkl	0*kl*	*h*0*l*	*hk*0	*h*00	0*k*0	00*l*	Space group from Table 3.2, ITC (7)
$h + l$	*k*,*l*	$h + l$	*h*	*h*	*k*	*l*	*Bbmm* (#63, *Cmcm*, *bca*), centrosymmetric $Bb2_1m$ (#36, $Cmc2_1$, *bca*), noncentrosymmetric *Bbm*2 (#40, *Ama*2, *bac*), noncentrosymmetric

Note. The space group symbols are given in coordinates of the drawing in Fig. 5 (in parentheses, standard setting and relationship between axes).

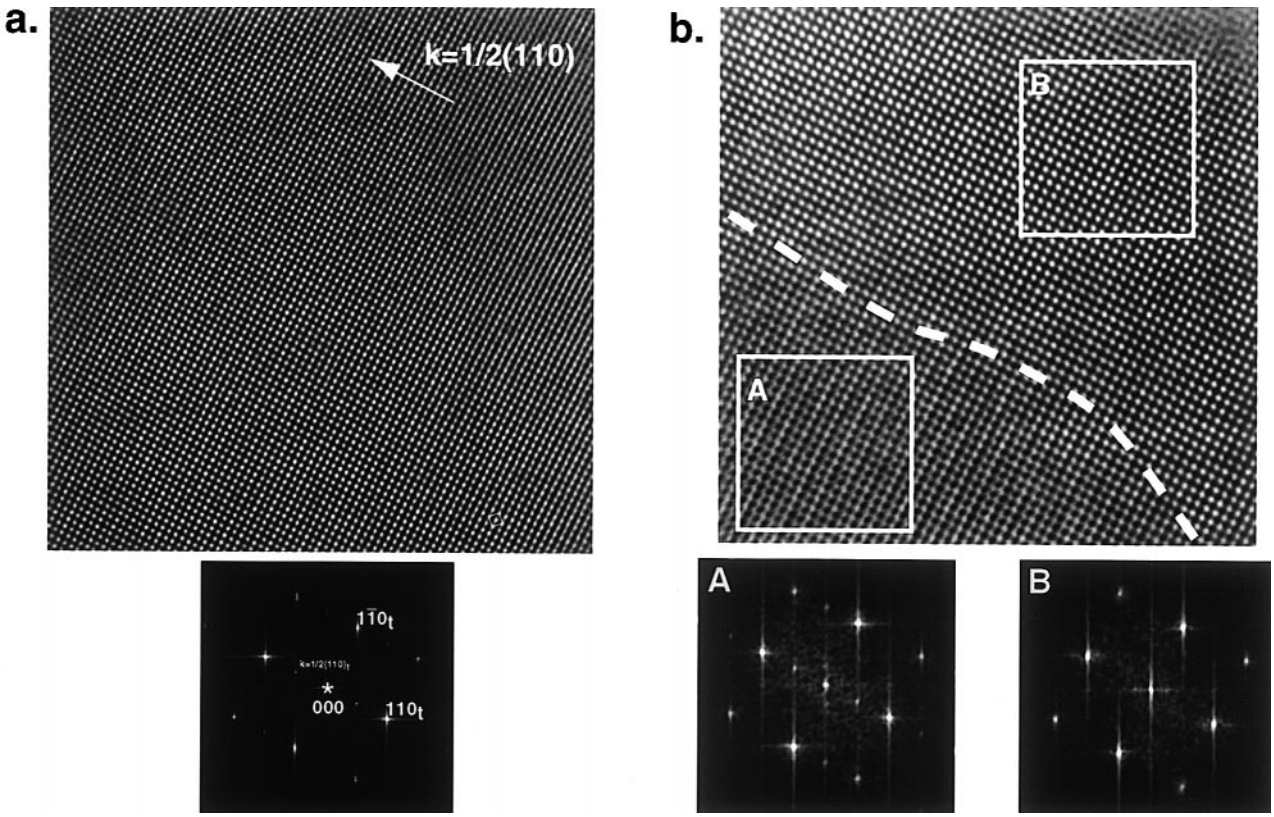

FIG. 6. HRTEM images taken from a $La_{2-2x}Ca_{1+2x}Mn_2O_7$ ($x = 0.85$) specimen at the $[001]_t$ orientation. (a) A single ordered domain with the corresponding FFT diffraction pattern in the inset showing $k = \frac{1}{2}(110)$ intensities. (b) A region showing the coexistence of ordered (A) and disordered (B) regions, as confirmed by the corresponding FFT calculated from the squared areas shown in the images.

occurring when the material is rapidly cooled from the temperature of sintering (1250°C) to RT. Therefore, both cooling and heating *in situ* TEM experiments were performed for the $x = 0.85$ and 0.9 specimens. In the cooling experiment the specimens were cooled to liquid N_2 temperature. No changes in the SAD pattern, or in the microstructure, were observed. In the heating experiments, the disappearance of superlattice reflections was observed around 200°C (temperature controller reading) for the $x = 0.9$ specimen, and around 340°C for the $x = 0.85$ specimen. Figure 11 shows a series of $[001]_t$ SAD patterns taken at different temperatures from a single grain of the $x = 0.9$ specimen. The disappearance/reappearance of $\frac{1}{2}[110]_t^*$ reflections on heating/cooling suggests a reversible (and therefore equilibrium) phase transition. Formation of diffuse reflections at $\frac{1}{4}(110)_t$ is possibly due to some compositional changes in a thin area of the TEM specimen.

The evolution of a row of $(\frac{1}{2}\ \frac{1}{2}\ l)_t$ superlattice reflections for the $x = 0.85$ specimen was studied along the $[110]_t$ orientation of a grain (Fig. 12). Again, the disappearance/reappearance of the superlattice reflections during the heating/cooling cycling is clear; however, the temperature of disappearance is higher for the $x = 0.85$ than $x = 0.9$ sample. Figure 13 shows the measured distribution of intensity along the AA' line, Fig. 13a, connecting the $(\bar{2}00)_o$ and $(202)_o$ reflections. Figure 13b shows the evolution of intensity as a function of temperature for two superlattice reflections, $(\bar{1}01)_o$ and $(103)_o$. Note that $(\bar{1}01)_o$ is systematically weaker than $(103)_o$. In Fig. 13c values of the intensities are plotted as a function of temperature. The gradual change in intensity with approaching the temperature of transition is apparent for both reflections.

4. DISCUSSION

All the studied $La_{2-2x}Ca_{1+2x}Mn_2O_7$ compounds for the $0.8 < x < 1.0$ composition range indicate the presence of a $n = 2$ RP single phase with an apparent orthorhombic structure at RT. However, for each sample, in addition to the crystalline phase a various amount ($\sim$5–15%) of an amorphous phase is also present. Qualitative analysis of the amorphous phase indicates the presence of all the atoms (i.e., La/Ca/Mn/O) of the starting composition (plus carbon); therefore, the compositions of the crystalline phases studied here slightly deviate from the "nominal" compositions.

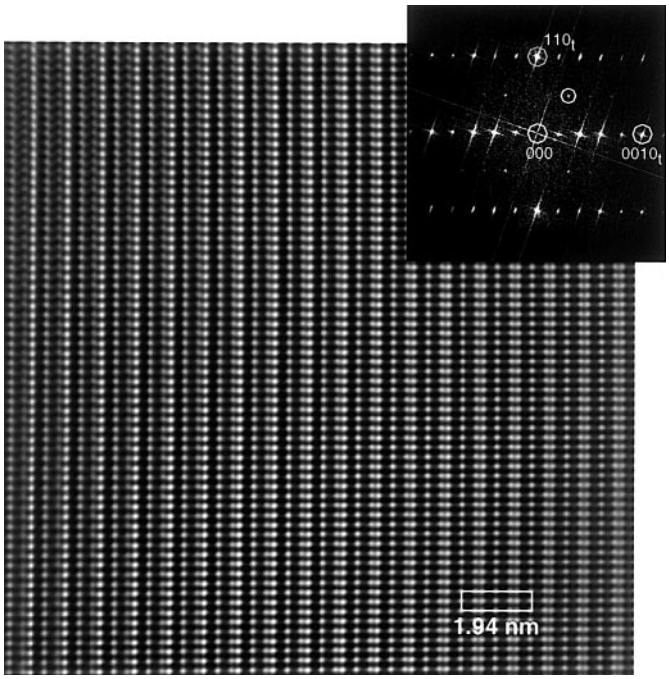

FIG. 7. HRTEM image ($x = 0.85$ specimen) in the $[1\bar{1}0]_t$ orientation showing perfect stacking of octahedra. Doubling of periodicity due to the $k = \frac{1}{2}\langle 110\rangle_t^*$ ordering can be seen only with the help of FFT shown as the inset.

According to the *in situ* experiment and microstructural observations, there is a structural transformation from the high-temperature ideal RP $I4/mmm$ phase. The temperatures of the transformations were determined only approximately. They appear to decrease with increasing Ca content, e.g., from 300°C for $x = 0.85$ to 200°C for $x = 0.9$, possibly due to the increase in tolerance factor for slightly larger Ca^{2+} ions. Note that the structural transition temperature is significantly higher than that observed by magnetic measurements, as described in Ref. (5). The transformation results in two structural variants, with ordering vectors $k_1 = \frac{1}{2}[110]_t^*$ and $k_2 = \frac{1}{2}[1\bar{1}0]_t^*$. An additional transformation, not detected in the *in situ* experiment, is possible and apparently results in the loss of inversion center and in the formation of inversion twins. It is difficult to detect the secondary transformation *in situ*, because it does not lead to clear changes in the reciprocal lattice.

The lattice parameters of the orthorhombic structure are related to the tetragonal RP structure by $a_o = \sqrt{2}a_t = 0.52$ nm; $b_o = \sqrt{2}a_t = \approx 0.52$ nm; $c_o = c_t = 1.93$ nm. Three possible space groups correspond to the experimentally observed reflection extinction conditions: $Bbmm$, $Bb2_1m$, and $Bbm2$ (in coordinates of the reciprocal lattice shown in Fig. 5). The standard setting for $Bbmm$ is $Cmcm$ (#63), and the axes in Fig. 5 are parallel to the following axes in standard setting: $a//b_s$, $b//c_s$, $c//a_s$. For the $Bb2_1m$ space group, the standard setting is $Cmc2_1$ (#36), with the

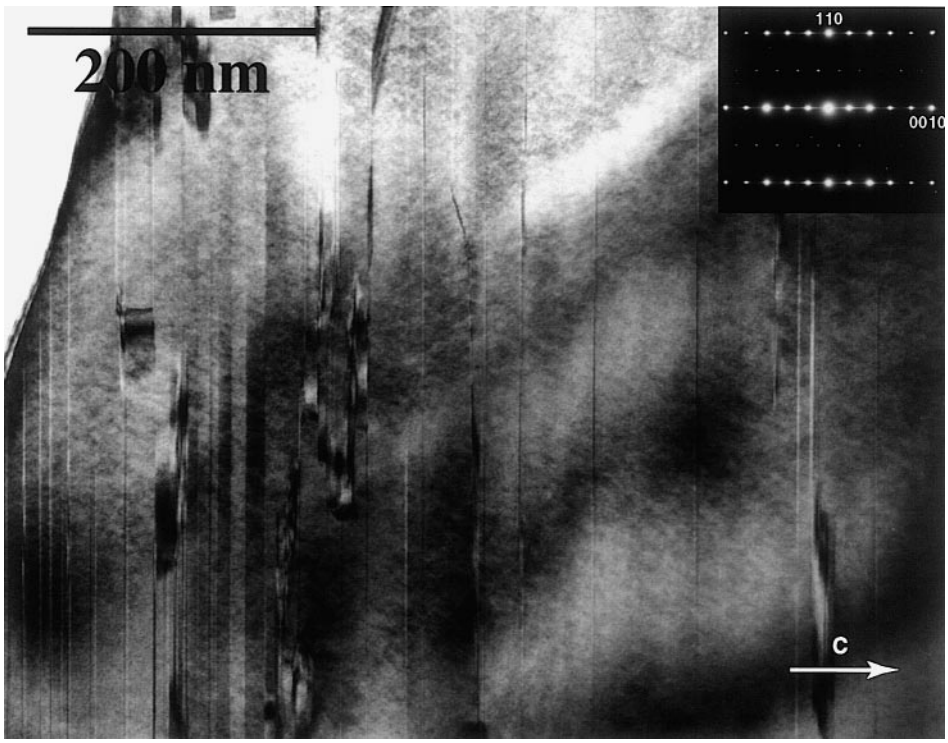

FIG. 8. Bright-field image of $x = 0.9$ specimen in the $[1\bar{1}0]_t$ orientation (with the inset showing the corresponding SAD pattern showing predominantly $n = 2$ structure). Planar defects normal to the $[001]_t$ are stacking faults and intergrowth blocks corresponding to mistakes in the packing of perovskite layers.

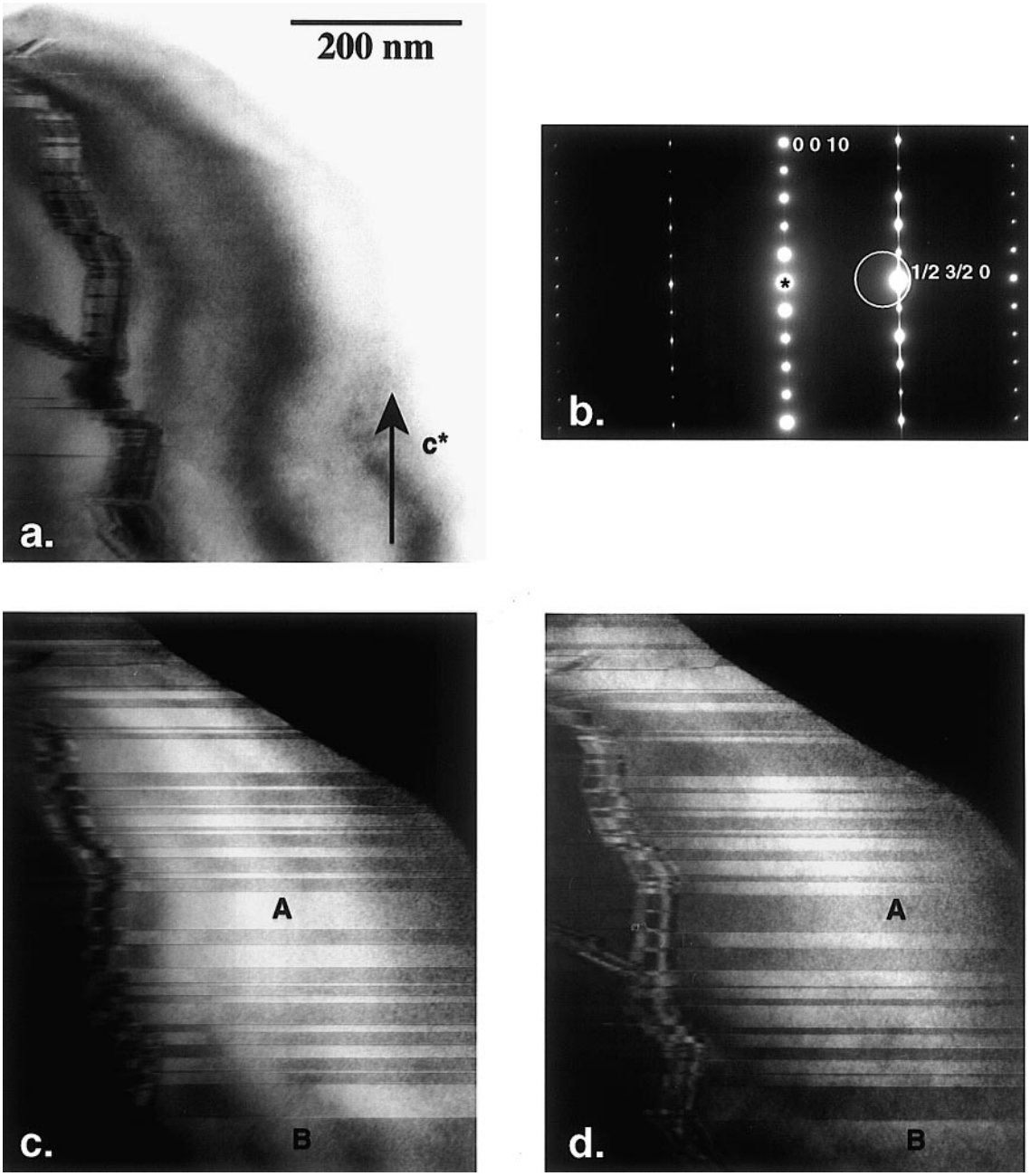

FIG. 9. (a) Bright-field and (c, d) two dark-field images taken from an $x = 0.85$ specimen in nearly $[320]_t$ orientation. For the dark-field images, an objective aperture was positioned as shown in the double-exposed $[320]_t$ SAD pattern (b). The difference in the conditions under which the two dark-field images were obtained is in a slight displacement of the aperture, which results in reversing the contrast of twins (e.g., A and B lamellae).

following axial correspondents: $a//b_s$, $b//c_s$, $c//a_s$. For the *Bbm*2 space group, the stanard setting is *Ama*2 (#40), with axial correspondents: $a//b_s$, $b//a_s$, $c//c_s$. Formally, the following maximal subgroup relationships between the space groups can be established: $I4/mmm$ (#139) $\Rightarrow$ [2] $\Rightarrow$ $Fmmm \Rightarrow$ [2] $\Rightarrow$ *Bbmm* (*Cmcm*, #63) $\Rightarrow$ [2] $\Rightarrow Bb2_1m$ ($Cmc2_1$, #36)[2] and $I4/mmm$ (#139) $\Rightarrow$ [2] $\Rightarrow Fmmm \Rightarrow$ [2] $\Rightarrow$ *Bbmm* (*Cmcm*, #63) $\Rightarrow$ [2] $\Rightarrow$ *Bbm*2 (*Ama*2, #40). The space groups $Cmc2_1$ and *Ama*2 are noncentrosymmetric. Therefore, it is plausible to infer that one of these symmetries represents the space group of a room

[2] Squared parentheses give the number of structural variants for each symmetry reduction.

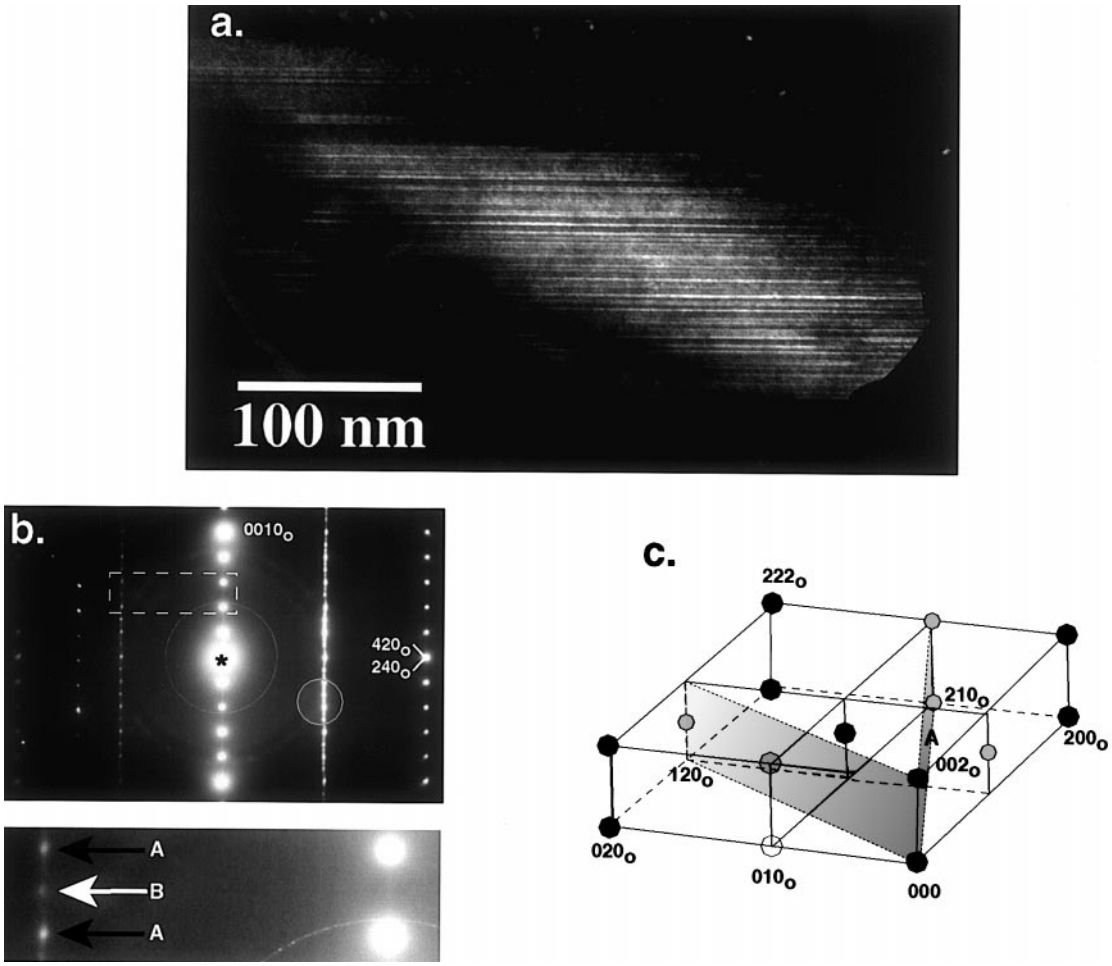

FIG. 10. (a) Dark-field image showing twinlike structure and (b) the corresponding SAD pattern ($x = 0.85$ specimen). The position of the objective aperture is indicated on the pattern. Enlargement of a part of the SAD pattern (b) shows the presence of superlattice reflections with both odd (A) and even (B) *l*. (c) Schematic drawing of the reciprocal lattice showing sections corresponding to patterns of A and B types.

temperature structure, and the transition from the *Cmcm* structure results in the formation of inversion domains (two variants by the symmetry reduction). The transition from tetragonal *I*4/*mmm* to orthorhombic *Cmcm* occurs at around 200–300°C, as detected by our *in situ* measurements. However, it is also probable that there is a single transition $I4/mmm \Rightarrow Cmc2_1$ or *Ama*2.

Since the RP structures consist of perovskite layers, it is possible that structural displacive instabilities typical for the infinite (3D) perovskites will also be present in the layered structure. One of the most common instabilities is the rotation/tilt of corner-sharing octahedra, related to the size misfit between *A*-type and *B*-type ions (8). Another possibility is the ordering of Mn^{3+} and Mn^{4+} ions accompanied by the Jahn–Teller instability of Mn^{3+} octahedra (9). The latter scenario seems unlikely, because of the difficulty of reconciling the ratio of $Mn^{3+}/Mn^{4+} = (1-x)/x < 0.25$ with the requirement that the $\frac{1}{2}[110]^*_t$-type ordering vector ratio be $\frac{1}{2}$. Structural phase transitions approximated as a tilt of rigid octahedra occur in different perovskite-based structures (e.g., elpasolites, ReO_3-type, etc.), and in particular in $CaMnO_3$ (10). The effect of the tilt (or combination of tilts) on symmetry (space group) was analyzed for infinite perovskites by Glazer (11) and Aleksandrov (10). Later the analysis was extended to different perovskite-based structures, including different layered structures (12). In particular, a complete symmetry analysis of Ruddlesden–Popper structures was presented recently by Aleksandrov and Bartolome (13) for all possible combinations of tilts in structures with layers consisting of even numbers of octahedra.

Consulting the derived space groups in (13), we find from the experimentally established space groups that the *Bbmm* (*Cmcm*) space group corresponds to a structure with ΦΦ0/ΦΦ0 combination of tilts ($a^-\ a^-\ 0/a^-\ a^-\ 0$ in Glazer's notations). In the notation used here, the Φ/a^- symbols represent an alternating tilt of an octahedron along a tilt

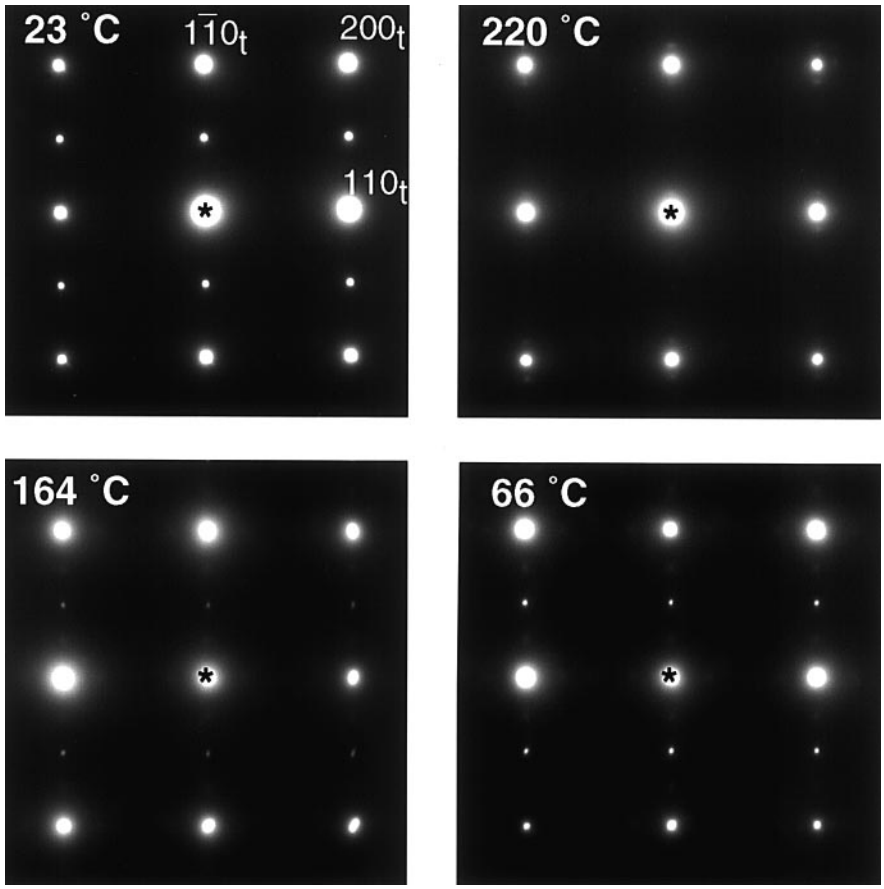

FIG. 11. Series of $\langle 001\rangle_t$ SAD patterns taken at different temperatures during the *in situ* heating experiment for the $x = 0.9$ specimen. The reappearance of $\frac{1}{2}(1\bar{1}0)_t$ reflections on cooling is accompanied with the formation of additional diffuse reflections, approximately at $\frac{1}{4}(1\bar{1}0)_t$.

axis. Figure 14 shows that the ΦΦ combination of tilts results in a tilt around a two-fold axis (normal to the *c*-axis) of an octahedron. For the ΦΦ0/ΦΦ0 structure in each layer the combination, the phase, and the degree of the tilt are the same. Figure 15 shows a schematic drawing of both *I*4/*mmm* (Fig. 15a) and *Bbmm* (*Cmcm*) (Fig. 15c) structures (the simplified representation using disjoined octahedra and no *A*-sites is adopted from Ref. (13)). The intermediate (formal and nonexistent) *Fmmm* structure is also shown for completeness (Fig. 15b). From the drawing of Fig. 15, the correspondence between some of the symmetry elements and the lattice origin is clear. Table 2 gives the evolution of Wyckoff positions of atoms from the ideal, nondistorted *I*4/*mmm* (positions are taken for $Ca_3Mn_2O_7$, Fawcett *et al.* (4)), to tilted *Cmcm* (through undistorted *Fmmm* and *Cmcm* with all atoms on the *I*4/*mmm* positions). The combined tilt ϕ (around an axis parallel to the *c*-axis) is approximated by adding parameters $\Delta_x = [(\sqrt{2}/4)\, a_p \text{ tg } \phi]/c_t = 0.07 \text{ tg } \phi$ and $\Delta_y = (\frac{1}{2})a_p \text{ tg } \phi/\sqrt{2}a_p = \text{tg } \phi/(2\sqrt{2})$ to the coordinates of oxygen atoms as shown in Table 2.

Considering the $Cmc2_1$ space group, according to Ref. (13) the symmetry agrees with a tilted structure with the $\Phi\Phi\Psi_z/\Phi\Phi\Psi_z$ combination of tilts. In this structure an additional tilt Ψ_z around the *c*-axis is added to the ΦΦ0/ΦΦ0 structure; a schematic drawing of the structure is shown in Fig. 15d. The Ψ_z symbol describes an in-phase tilt of octahedra around the four-fold axis of the octahedra parallel to the long *c*-axis (normal to a layer's plane). Therefore, the suspected secondary transition may result in adding the tilt Ψ_z to an already tilted structure. That transition can introduce a set of inversion twins, which are structurally different only by the sense of the tilt Ψ_z (right- and left-handed). The observed $(001)_t$ interfaces between the inversion twins (within the same *Cmcm* variant) should be of very low energy, with a perfect match along the interface. Displacement of O(2) and O(4) oxygen atoms of the *Cmcm* structure, as shown in the last column of Table 2, approximates the Ψ_z tilt. Displacement parameters δ_z and δ_y are related to the tilt angle as $\delta_z = (\sqrt{2}/4)a_p \sin \Psi_z/\sqrt{2}a_p = \sin \Psi_z/4$ and $\delta_y = (\sqrt{2}/4)a_p(\cos \Psi_z - 1)/\sqrt{2}a_p = (\cos \Psi_z - 1)/4$.

As for *Bbm*2 (*Ama*2, #40), no combination of tilts satisfying the space group and the lattice could be found in Ref. (13). The $\Psi 0\Psi_z/0\Psi\Psi_z$ and $\Psi\Psi\Psi_z/\underline{\Psi\Psi}\Psi_z$ combinations of tilts are possible in *Ama*2, but this structure has

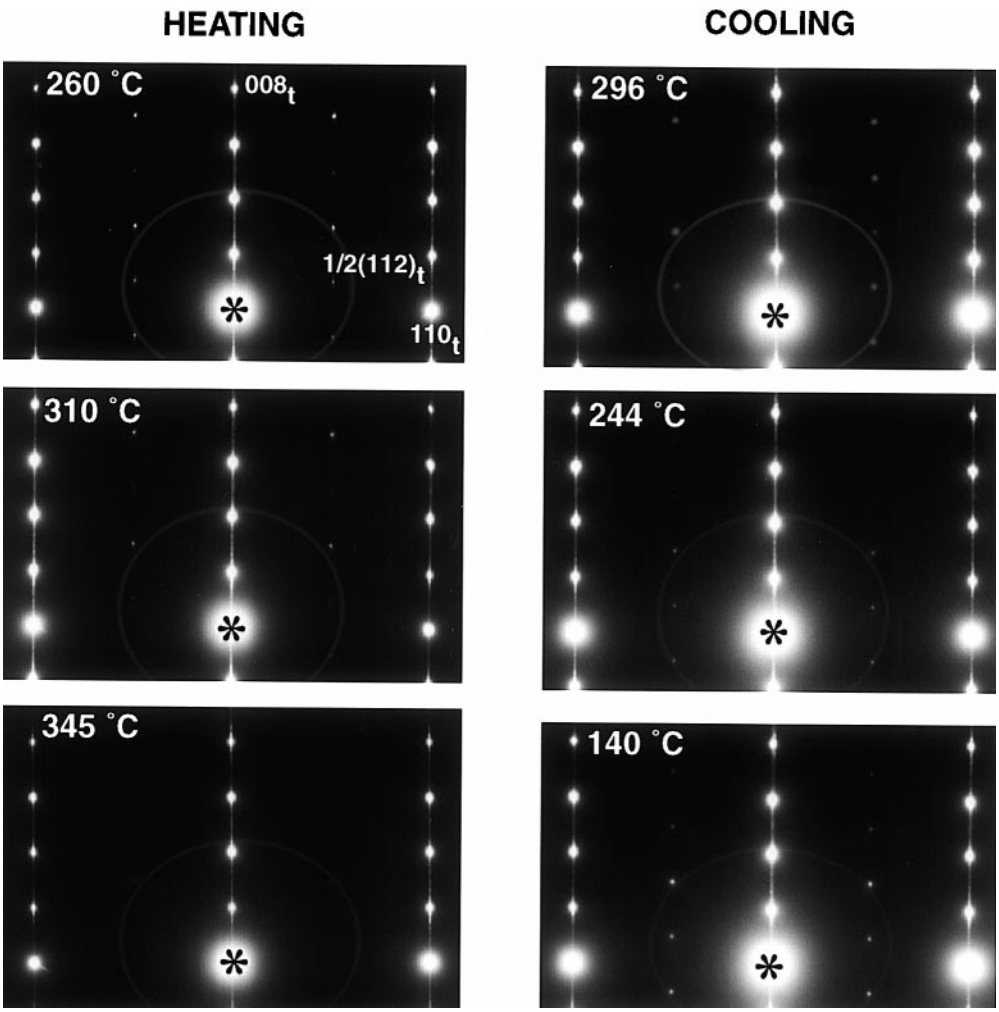

FIG. 12. Series of $\langle 110 \rangle_t$ SAD patterns taken at different temperatures during the *in situ* heating experiment for the $x = 0.85$ specimen.

$2\sqrt{2}a_p \times 2\sqrt{2}a_p$ yielding a cell twice that of the experimental one. These combinations of tilts cannot be developed directly from the ΦΦ0/ΦΦ0 structure of *Cmcm*. A structural model involving *Ama*2, when considered as a further symmetry reduction of the ΦΦ0/ΦΦ0 structure, will lack mirror and glide planes normal to the long axis. This implies distortions, which render the connected octahedra within a layer (octahedra with different z) nonidentical. Thus it appears that a model using the $Cmc2_1$ space group and a $\Phi\Phi\Psi_z/\Phi\Phi\Psi_z$ combination of tilts is more plausible than the result derived using *Ama*2.

Although it is difficult to provide a quantitative analysis of the model using only results of dynamic electron scattering, comparison with kinematic reflections, e.g., of X-ray scattering, can provide some useful information. Therefore we calculated the intensity of superlattice X-ray reflections as a function of a combined tilt, ϕ, for the *Bbmm* (*Cmcm*) ΦΦ0/ΦΦ0 structure. Figure 16 shows a plot of the intensities for $(101)_o$ and $(103)_o$ reflections and ϕ ranging from 0 to 15°. The variation is similar to the dependence of intensity of these reflections (from electron diffraction, Figs. 12 and 13) on temperature. The intensity of the $(101)_o$ reflection is stronger than that of the $(103)_o$, which is evident from the electron diffraction, and even more so from the FFT high-resolution image (e.g., in Fig. 8). Changing the structure to $Cmc2_1$ with $\Phi\Phi\Psi_z/\Phi\Phi\Psi_z$ combination of tilts (for $\Psi_z = 15°$) does not contribute significantly to the intensity (see the filled square/circle in Fig. 16). We hope that an ongoing study of the structure using powder neutron diffraction will clarify whether the suggested models are correct. However, the presence of partial intergrowth, as well as twins and possible disorder in the phase of octahedra tilt in different layers, may make the final judgement difficult.

The RP structure with $n = 2$ and $\Phi\Phi\Psi_z/\Phi\Phi\Psi_z$ combination of tilts has been reported thus far only for one oxide, $Ca_3Ti_2O_7$ (14). This structure was studied in detail by

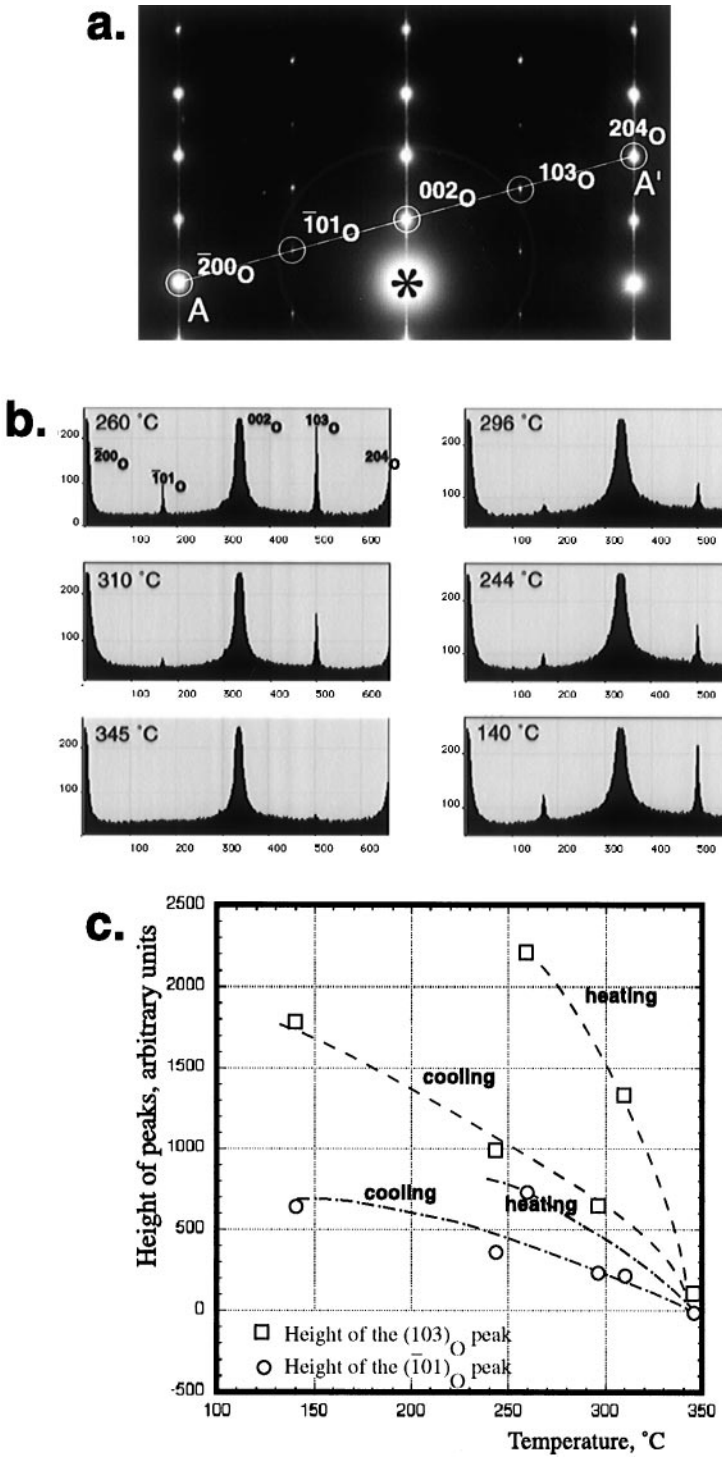

FIG. 13. Measured distribution of intensity along the AA′ line, connecting $[\overline{2}00]_o$ and $(204)_o$ (o, orthorhombic indexes) reflections on the $[110]_t$ SAD pattern (a) (same as in the previous figure). (b) Evolution of the intensity for two superlattice reflections, $(\bar{1}01)_o$ and $(103)_o$. (c) Values of the $(\bar{1}01)_o$ and $(103)_o$ intensities are plotted as a function of temperature for a heating/cooling cycle.

electron microscopy and powder neutron diffraction with the refinement determined value of the Φ and Ψ_z tilts as 9.7° and 8.6°, respectively. Bismuth-based oxides with Aurivillius-type structure (closely related to the RP type) with $n = 2$, $Bi_2SrNb_2O_9$, $Bi_2SrTa_2O_9$, and Bi_3TiNbO_9 (15, 16), were also identified by Aleksandrov and Bartolome (13) as having the $\Phi\Phi\Psi_z/\Phi\Phi\Psi_z$ tilt structure. Phase transitions were not studied for these structures. A modification RP

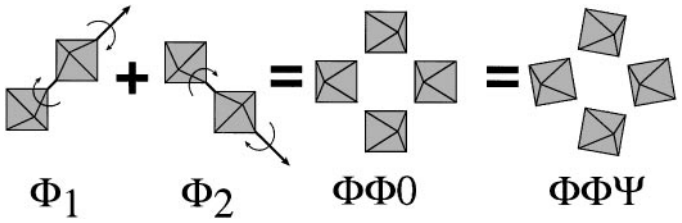

FIG. 14. Schematic drawing showing the ΦΦ combination of tilts resulting in a tilt around the two-fold axis (normal to the *c-axis*) of an octahedron.

structure (with tetrahedral sites instead of a rock salt layer) was studied for $Li_2Sr_{n-1}M_nO_{3n+1}$ (M = Nb, Ta) and identified as having *Cmcm* space group and ΦΦ0/ΦΦ0 ilts (17). Therefore, our model of $\Phi\Phi\Psi_z/\Phi\Phi\Psi_z$ tilts for $La_{2-2x}Ca_{1+2x}Mn_2O_7$ ($0.8 \leq x \leq 1.0$) is not unusual, although the first is suggested for manganites.

The evolution of intensities of superlattice peaks (although very qualitative), as measured from SAD micrographs taken at different temperatures, suggests

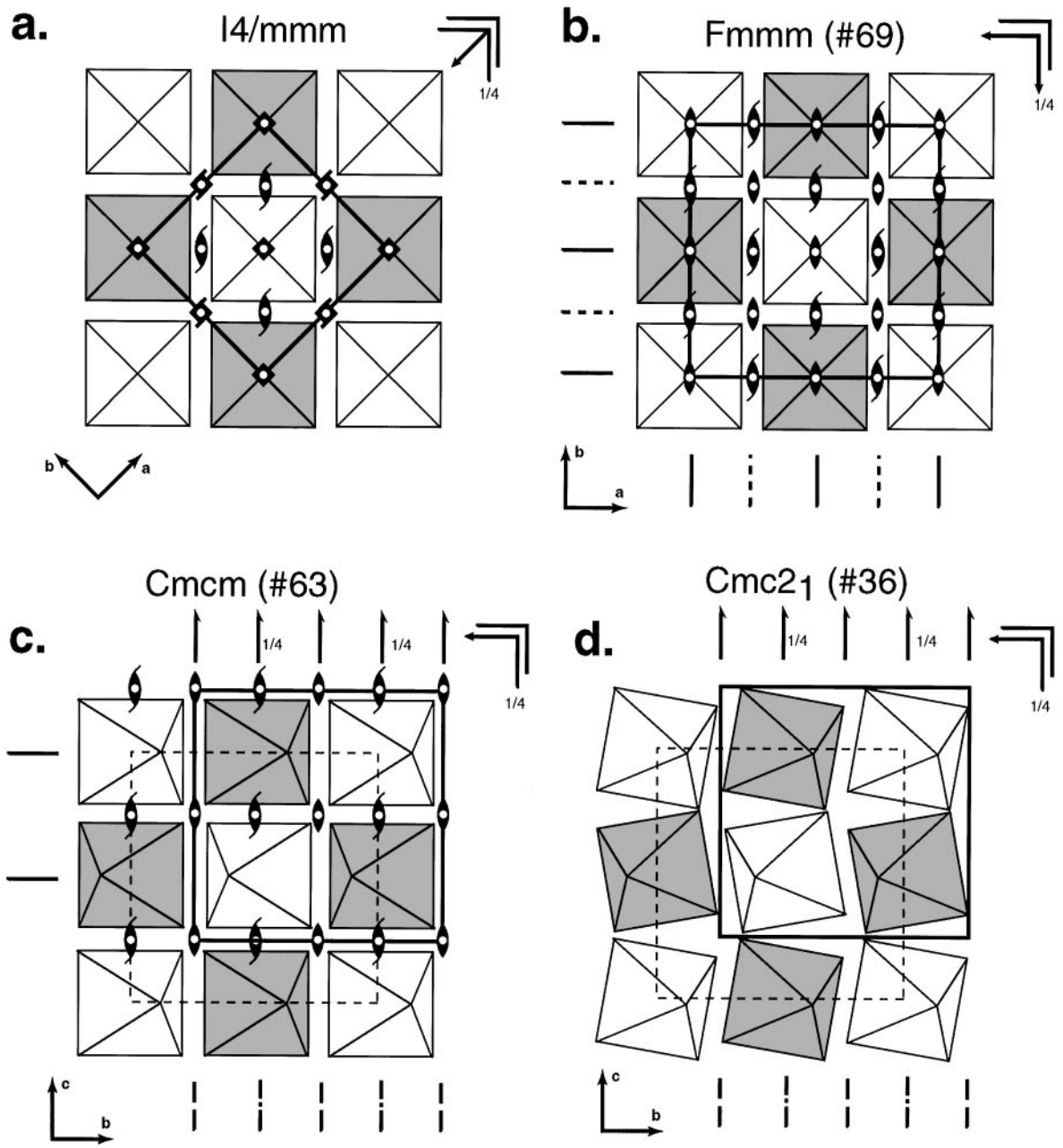

FIG. 15. Schematic drawings of (a) *I*4/*mmm*, (b) *Fmmm*, (c) *Bbmm* (*Cmcm*), and (d) *Bb*2_1*m* (*Cmc*2_1) structures with (a, b) no tilt, (c) ΦΦ0/ΦΦ0, and (d) $\Phi\Phi\Psi_z/\Phi\Phi\Psi_z$ combination of tilts. In drawing the simplified representation using disjoined octahedra and no A sites is adopted from Ref. (14). The shaded and empty octahedra represent two adjacent perovskite layers. The correspondence between some of the symmetry elements, lattices, and lattice origin is shown.

TABLE 2
Evolution of Coordinates from Nontilted *I4/mmm* to Tilted $\Phi\Phi\Psi_z/\Phi\Phi\Psi_z$ $Ca_3Mn_2O_7$ Structure

*I*4/*mmm*, untilted	*Fmmm* #69, untilted	*Cmcm* #63, untilted	*Cmcm* #63, tilted ΦΦ0/ΦΦ0	*Ccm*2$_1$ #36, tilted $\Phi\Phi\Psi_z/\Phi\Phi\Psi_z$
$a_t = 3.73$ (a_p) Å $b_t = 3.73$ (a_p) Å $c_t = 19.37$ Å	$a = 5.27 = \sqrt{2}a_p$ $b = 5.27 = \sqrt{2}a_p$ $c = 19.37$ Å	$a = 19.37$ Å b = $5.27 = \sqrt{2}a_p$ $c = 5.27 = \sqrt{2}a_p$	$a = c_t = 19.37$ Å $b = 5.27 = \sqrt{2}a_p$ $c = 5.27 = \sqrt{2}a_p$	$a = 19.37$ Å $b = 5.27 = \sqrt{2}a_p$ $c = 5.27 = \sqrt{2}a_p$
Ca(1) 2*b* (0, 0, $\frac{1}{2}$)	Ca(1) 4*b* (0, 0, $\frac{1}{2}$)	Ca(1) 4*c* ($\frac{1}{2}$, $-\frac{1}{4}$, $-\frac{1}{4}$) (0, *y*, $\frac{1}{4}$)	Ca(1) 4*c* ($\frac{1}{2}$, $-\frac{1}{4}$, $-\frac{1}{4}$)	Ca(1) 4*a* ($\frac{1}{2}$, $-\frac{1}{4}$, $-\frac{1}{4}$)
Ca(2) 4*e* (0, 0, 0.31)	Ca(1) 8*i* (0, 0, 0.31)	Ca(1) 8*g* (0.31, $-\frac{1}{4}$, $-\frac{1}{4}$) (*x*, *y*, $\frac{1}{4}$)	Ca(1) 8*g* (0.31, $-\frac{1}{4}$, $-\frac{1}{4}$)	Ca(1) 8*b* (0.31, $-\frac{1}{4}$, $-\frac{1}{4}$)
Mn 4*e* (0, 0, 0.098)	Mn 8*i* (0, 0, 0.098)	Mn 8*g* (0.098, $-\frac{1}{4}$, $-\frac{1}{4}$) (*x*, *y*, $\frac{1}{4}$)	Mn 8*g* (0.098, $-\frac{1}{4}$, $-\frac{1}{4}$)	Mn 8*b* (0.098, $-\frac{1}{4}$, $-\frac{1}{4}$)
O(1) 2*a* (0, 0, 0)	O(1) 4*a* (0, 0, 0)	O(1) 4*c* (0, $-\frac{1}{4}$, $-\frac{1}{4}$) (0, *y*, $\frac{1}{4}$)	O(1) 4*c* (0, $-\frac{1}{4}+\Delta_y$, $-\frac{1}{4}$)	O(1) 4*a* (0, $-\frac{1}{4}+\Delta_y$, $-\frac{1}{4}$)
O(2) 8*g* (0, 0.5, 0.0871)	O(2) 16*j* ($\frac{1}{4}$, $\frac{1}{4}$, 0.0871)	O(2) 8*e* (0.0871, 0, 0) (*x*, 0, 0)	O(2) 8*e* (0.0871+Δ_x, 0, 0)	O(2) 8b (0.0871+Δ_x, 0+δ_y, 0−δ_z)
		O(4) 8*e* (0.0871, 0.5, 0) (*x*, 0, 0)	O(4) 8*e* (0.0871−Δ_x, 0.5, 0)	O(4) 8b (0.0871−Δ_x, 0.5−δ_y, 0+δ_z)
O(3) 4*e* (0, 0, 0.2047)	O(3) 8*i* (0, 0, 0.2047)	O(2) 8*g* (0.205, $-\frac{1}{4}$, $-\frac{1}{4}$) (*x*, *y*, $\frac{1}{4}$)	O(2) 8*g* (0.205, $-\frac{1}{4}-\Delta_y$, $-\frac{1}{4}$)	O(2) 8*b* (0.205, $-\frac{1}{4}-\Delta_y$, $-\frac{1}{4}$)

a gradual change in the order parameter, and therefore the possibility of a second-order transition. Group theoretical analysis shows that the suggested reduction in symmetry corresponds to the following changes in point group symmetry: $4/mmm \Rightarrow mmm \Rightarrow mm2$ (for both *Cmc*2$_1$ and *Ama*2 space groups). In this transition the number of atoms in the primitive unit cell does not change. Indenbom (18) has analyzed such transformations by group theoretical methods in order to identify the possible second-order transitions. According to that analysis, the transitions from the ideal *I*4/*mmm* to either *Cmcm* or *Cmc*2$_1$ and *Ama*2 can be second order.

5. CONCLUSIONS

A series of Ruddlesden–Popper compounds with $n = 2$ and stoichiometry $La_{2-2x}Ca_{1+2x}Mn_2O_7$ synthesized by a citrate gel technique have been studied by TEM for the composition range $0.8 \leq x \leq 1.0$. *In situ* experiments and microstructural analysis identified structural changes of the *I*4/*mmm* phase at low temperatures (200–350°C). The low-temperature phase is noncentrosymmetric with either *Cmc*2$_1$ or *Ama*2 space group, and the transient *Cmcm* space

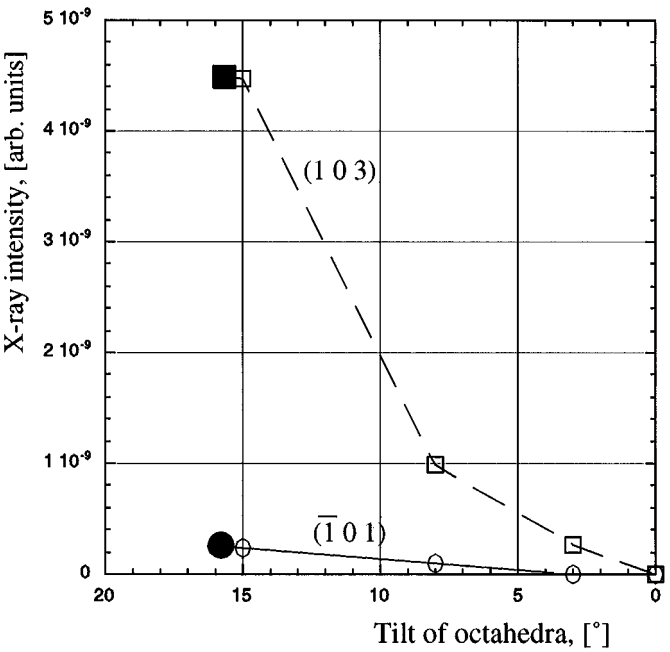

FIG. 16. Plot of the intensities for $(\bar{1}01)_o$ and $(103)_o$ reflections for a tilt angle ϕ ranging from 0 to 15°. The intensities were calculated for X-ray scattering using *Cmcm* (empty square/circle) and *Cmc*2$_1$ (filled square/circle) structure with $\Psi_z = 15°$.

group is also possible. These structural transitions do not coincide with the magnetic transitions. A structural model based on tilting of almost-rigid octahedra was suggested for *Cmcm* and $Cmc2_1$. The model for the low-temperature $Cmc2_1$ phase has a $\Phi\Phi\Psi_z/\Phi\Phi\Psi_z$ combination of tilts. Further neutron diffraction experiments to verify the validity of the model are in progress.

REFERENCES

1. C. N. R. Rao, A. K. Cheetham, and R. Mahesh, *Chem. Mater.* **8,** 2421 (1996) and references therein.
2. S. N. Ruddlesden and P. Popper, *Acta Crystallogr.* **11,** 541 (1958).
3. Y. Moritomo, A. Asamitsu, H. Kuwahara, and Y. Tokura, *Nature* **380,** 141 (1996); A. M. Goldman, *Science* **274,** 1630 (1996); T. Kimura, Y. Tomioka, H. Kuwahara, A. Asamitsu, M. Tamura, and Y. Tokura, *Science* **274,** 1698 (1996).
4. H. Asano, J. Hayakana, and M. Matsui, *Phys. Rev. B* **56,** 5345 (1997); D. Fawcett, J. E. Sunstrom IV, M. Greenblatt, M. Croft, and K. V. Ramanujachary, *Chem. Mater.* **10,** 3643 (1998).
5. D. Fawcett, M. Greenbalt, M. Croft, and L. A. Bendersky, *Phys. Rev. B* **62,** 62 (2000).
6. L. A. Bendersky, R. C. Chen, and M. Greenblatt, unpublished.
7. "International Tables for Crystallography" (T. Hahn, Ed.). Reidel, Dordrecht, 1987.
8. P. M. Woodward, *Acta Crystallogr. B* **53,** 32 (1997); *Acta Crystallogr. B* **53,** 44 (1997).
9. C. N. R. Rao, A. Aruiraj, P. N. Santosh, and A. K. Cheethman, *Chem. Mater.* **10,** 2714 (1998); S.-W. Cheong and H. Y. Hwang, *in* "Colossal Magnetoresistance Oxides" (Y. Tokura, Ed.), Gordon & Breach, Monograph in Condensed Matter Science, in press.
10. K. S. Aleksandrov, "Perovskitopodobnie kristalli." Novosibirsk, Nauka, Moscow, 1997 (in Russian).
11. M. Glazer, *Acta Crystallogr. B* **28,** 3385 (1975).
12. R. Deblieck, *et al.*, *Acta Crystallogr. B* **41,** 319 (1985); K. S. Aleksandrov, *Sov. Phys. Crystallogr.* **32,** 387 (1987); I. Levin and L. A. Bendersky, *Acta Crystallogr. B* **55,** 853 (1999).
13. K. S. Aleksandrov and J. Bartolome, *J. Phys. Condens. Matter* **6,** 8219 (1994).
14. M. M. Elcombe, E. H. Kisi, K. D. Hawkins, T. J. White, P. Goodman, and S. Matheson, *Acta Crystallogr. B* **47,** 305 (1991).
15. D. Rae, J. G. Thompson, and R. L. Whither, *Acta Crystallogr. B* **48,** 418 (1992).
16. J. G. Thompson, A. D. Rae, R. L. Whither, and D. C. Craig, *Acta Crystallogr. B* **47,** 174 (1991).
17. N. Floros, C. Michel, M. Hervieu, and B. Raveau, *J. Mater. Chem.* **9,** 3101 (1999).
18. V. L. Indenbom, *Sov. Phys. Crystallogr.* **5,** 106 (1960).